BRILLOUIN STUDIES OF DIOPSIDE AND H_2O

BY

LIQIN SANG

THESIS

Submitted in partial fulfillment of the requirements
for the degree of Master of Science in Geology
in the Graduate College of the
University of Illinois at Urbana-Champaign, 2012

Urbana, Illinois

Adviser:

Professor Jay D. Bass

ABSTRACT

In chapter 1, we investigate the elastic properties of diopside, $CaMgSi_2O_6$, at ambient pressure and room temperature by Brillouin spectroscopy. The thirteen single-crystal elastic moduli (C_{ij}) of two samples of diopsidic pyroxenes close to the ideal composition from different locations have been measured. No unusual compositional dependence of C_{ij} values or the shear modulus near end-member diopside composition is observed.

In chapter 2, we further investigate the elastic properties of diopside at high pressure using a diamond anvil cell. The single-crystal elastic constants of diopside have been measured up to 14 GPa using Brillouin spectroscopy, from which the aggregate compressional and shear velocities, adiabatic bulk modulus, shear modulus and their pressure derivatives were obtained. This study not only provides the first high-pressure experimental data on the individual C_{ij}'s but also extends direct measurements on shear modulus for diopside to higher pressure than previous studies.

Chapter 3 describes the thermodynamic properties of H_2O. We determined the melting curve of Ice VII by simultaneous measurements of sound velocity and angle-dispersive synchrotron x-ray diffraction in a membrane-type diamond anvil cell with resistance heating at elevated temperatures to 873 K at pressures of 2 GPa to 14 GPa. We observed higher melting curves than previous studies, with the differences in melting temperature of ~120 K at 8 GPa. The sound velocity of liquid H_2O was measured up to 723K and 6.3 GPa. Measured sound speeds are significantly lower than previous acoustic measurements, with the discrepancy as high as 9% along 723K isotherm. A tentative equation of state (EOS) for liquid H_2O was obtained

with the velocity – pressure – temperature data. More sound velocity data at different pressure along several high-temperature isotherms is required for a more accurate estimate of the EOS.

ACKNOWLEDGEMENTS

I sincerely thank my adviser, Dr. Jay D. Bass for his continuous and tireless support and guidance during my graduate study at the University of Illinois. I wish to express profound gratitude for his support on my life decisions and careful work on my manuscripts. I also thank my labmates, namely Jin Zhang, Jia Chen, Guimiao Zhang and Seiji Kamada for laboratory assistance and useful discussions on my research. I acknowledge all the co-authors in my research paper and manuscripts, namely C.B. Vanpeteghem, S.V. Singeikin, D.L. Farber, C.R. Aracne, V. Prakapenka, I. Kantor, S. Tkachev and K. Zhuravlev. I gratefully acknowledge George Harlow (American Museum of Natural History, New York) for proving the Wakefield diopside sample, I. Steele and J. Jackson for the electron microprobe analyses and Sergey Tkachev for the neon gas loading of the diopside samples. Finally, I thank my family and friends for their support throughout this experience. The work described in chapter 1 and 2 was supported by the National Science Foundation under grant EAR-0738871, by the Consortium for Materials Properties Research in Earth Sciences (COMPRES) under NSF grant EAR-1043050. Funding for the study described in Chapter 3 was provided by the Department of Energy grant DE-FG02-08ER15961, NSF grant EAR0738871, and from COMPRES under cooperative agreement 10-43050.

TABLE OF CONTENTS

Chapter 1

The elastic properties of diopside at ambient pressure[1]

Abstract

The thirteen single-crystal elastic moduli of two samples of diopsidic pyroxenes close to the ideal composition ($CaMgSi_2O_6$) from different locations have been measured at ambient pressure and room temperature by Brillouin spectroscopy. We obtain (in GPa, ±1σ uncertainty): C_{11} = 229.0(4), C_{22} = 179.0(4), C_{33} = 242.5(4), C_{44} = 78.9(3), C_{55} = 68.1(2), C_{66} = 78.2(3), C_{12} = 78.0(7), C_{13} = 69.8(6), C_{23} = 58.0(7), C_{15} = 9.9(3), C_{25} = 6.1(5), C_{35} = 40.9(3), C_{46} = 6.6(2) and C_{11} = 226.1(9), C_{22} = 179.5(8), C_{33} = 239.2(9), C_{44} = 78.1(6), C_{55} = 69.2(4), C_{66} = 76.4(8), C_{12} = 77.4(10), C_{13} = 70.2(13), C_{23} = 56.7(16), C_{15} = 9.9(7), C_{25} = 5.9(12), C_{35} = 41.0(7), C_{46} = 6.8(4) for the two diopside samples. There are no major differences in the elastic tensor of the nearly pure diopside composition compared with the second sample containing slightly higher Al and Fe contents. Polycrystalline averaging of the C_{ij} for the bulk and shear moduli yield K_s = 114.6(7) GPa, G = 72.7(4) GPa, and K_s = 113.7(8) GPa, G = 72.2(5) GPa for the two diopside samples. The shear moduli reported here are 8% larger than those determined from previous

[1] The chapter is based on the paper: Sang, L.Q., Vanpeteghem, C.B., Sinogeikin, S.V., and Bass, J.D. (2011) The elastic properties of diopside, $CaMgSi_2O_6$. American Mineralogist, 96(1), 224-227.

measurements on a similar natural sample, but are in good agreement with recently reported values. We confirm the existence of systematic correlations between the composition of the M2 site and most of the C_{ij} values. No unusual compositional dependence of C_{ij} values or the shear modulus near end-member diopside composition is observed.

1.1. Introduction

Ca-rich clinopyroxene is considered to be one of the four major minerals in the Earth's upper mantle, along with olivine, orthopyroxene and pyrope-rich garnet. Because Ca-rich clinopyroxenes represent approximately 10 to 30 % of the upper mantle (McDonough 1990), they have been the subject of several previous studies of their elastic properties and phase relations (e.g., Levien et al. 1979; Levien and Prewitt 1981; Kandelin and Weidner 1988a; Zhang et al. 1989; Zhang and Hafner 1992; Comodi et al. 1995; Norris and Bass 2010). To accurately describe the seismic behavior of the Earth's mantle, it is necessary to understand the elastic properties of mantle minerals and their variation with pressure and temperature. Single-crystal elasticity measurements using Brillouin spectroscopy have been previously performed on monoclinic pyroxenes of various compositions at ambient conditions, such as near end-member compositions of jadeite (Kandelin and Weidner 1988b; Norris and Bass 2010), diopside (Levien et al. 1979) and omphacite (Bhagat et al. 1992).

Collins and Brown (1998) determined the elasticity of a natural clinopyroxene with composition $Di_{72}Hd_9Jd_3Cr_3Ts_{12}$ (Di, diopside; Hd, hedenbergite; Jd, jadeite; Cr, kosmochlor; Ts, Mg-Tschermakite) by the impulsive stimulated scattering technique. Their results brought to light some irregularities in the compositional dependence of C_{ij} along the diopside-jadeite join, in particular, unusual changes of C_{66} and C_{15} near the diopside end-member. More recently, Isaak and Ohno (2003) measured the elastic moduli of chrome-diopside from resonant ultrasound spectroscopy. They also noted unusual compositional dependence of the elastic constants near the diopside end member, in particular C_{66}, C_{13} and C_{15}, compared to the results of Levien et al. (1979). They proposed that this effect could be related partly to compositional variations in both M2 and M1 sites that are not taken into account when data are projected onto the Di: Jd join. In this study, we have re-investigated the elastic moduli of diopside at ambient conditions, employing improvements in Brillouin scattering techniques that have evolved since the previous diopside study carried out by Levien et al. (1979). The single-crystal elastic moduli can now be measured with far greater precision and accuracy than was possible even just a decade ago. In light of these new measurements, we reconsider the compositional dependence of elastic properties in the Di-Jd system.

1.2. Experimental Methods

Two different samples, diopside 1 (Wakefield, Quebec) and diopside 2 (DeKalb, New York), were used for this experiment. The dimensions of both these single crystals were approximately 1000 × 400 × 100 μm. Their compositions were determined by electron microprobe analysis (Table 1.1). Diopside 1 is very close in composition to the diopside end-member, while diopside 2 has slightly higher Fe and Al content.

Diopside has a monoclinic structure with space group C2/*c* (Warren and Bragg, 1928). The unit cell dimensions for diopside 1, as determined by a 4-circle x-ray diffractometer, are: a = 9.759(6), b = 8.933(5), and c = 5.256(3) Å, β = 105.852(7)°. This yields V_0 = 440.7(8) Å^3 and density ρ = 3.264(6) g/cm^3 for diopside 1. For diopside 2, a = 9.750(5), b = 8.923(5), and c = 5.255(3) Å, β = 105.85(1)°, yielding V_0 = 439.85(7) Å^3 and density ρ = 3.270(1) g/cm^3.

For each sample, we prepared three 25-30 μm thick crystals by polishing nearly parallel to *a*-*b*, *b*-*c* and *a*-*c* planes. The crystals were oriented by a four-circle x-ray diffractometer. The crystals were then mounted on a three-circle goniometer at the intersection of the optical axes of the Brillouin analysis system and the incident light. The orientations of the sample surfaces were checked using specular back reflections of light from growth faces with an accuracy of 0.5º or better.

The Brillouin measurements were made in air. An Ar laser (λ = 514.5 nm) was used as a light source, and the measurements were performed using a 90º scattering geometry with a 6-pass piezoelectrically scanned Fabry-Perot interferometer (Bass 1989; Sinogeikin et al. 1998). Acoustic velocities were determined from the results of Brillouin scattering measurements performed in 20 different crystallographic orientations.

1.3. Results

We determined the 13 adiabatic elastic constants that are necessary to fully characterize the elastic properties for monoclinic symmetry. The elastic constants are defined with references to three orthogonal axes, which correspond to the *a**, *b*, and *c*-axes. The Brillouin spectra showed one compressional and two shear modes for *a*-*b* and *b*-*c* planes, but for the *a*-*c* plane only one shear mode was observed. The results are shown in Figure 1.1.

A linearized inversion method (Weidner and Carleton 1977) was used to invert the acoustic velocities to determine the elastic moduli. The best fit produces a 20 m/s RMS (root mean square) error (difference between calculated and observed velocities) for diopside 1, and 26 m/s RMS error for diopside 2. Table 1.2 shows the values obtained for the elastic moduli of our samples compared to those of chrome-diopside (Isaak and Ohno 2003), and DeKalb diopside (Levien et al. 1979). The Voigt (V), Reuss (R) and Hashin-Shtrikman (HS^+, HS^-) bounds on the

aggregate bulk and shear moduli, K_s and G, respectively, were calculated from the single-crystal elastic moduli (Watt et al. 1976). For bulk modulus K_s(R) = 111.2(3) GPa, K_s (HS^-) = 114.1(3) GPa, K_s (HS^+) = 115.3(3) GPa, K_s (V) = 118.0(3) GPa for diopside 1; and K_s (R) = 110.4(5) GPa, K_s (HS^-) = 113.3(5) GPa, K_s (HS^+) = 114.4(5) GPa, K_s (V) = 117.0(5) GPa for diopside 2. For the shear modulus G, we found G(R) = 70.7(1) GPa, G (HS^-) = 72.3(1) GPa, G (HS^+) = 73.0(1) GPa, G (V) = 74.7(1) GPa for diopside 1 and G(R) = 70.3(3) GPa, G (HS^-) = 71.9(3) GPa, G (HS^+) = 72.5(3) GPa, G (V) = 74.1(3) GPa for diopside 2. The calculated errors for K_s and G (Table 1.2) consider the differences between the Hashin-Shtrikman bounds and statistical uncertainties of the individual C_{ij} (Watt et al. 1976).

1.4. Discussion

Table 1.2 shows a complete list of the elastic moduli obtained in the present study along with those of chrome-diopside (Isaak and Ohno 2003) and the results of Levien et al. (1979). The elastic moduli values of our two samples generally agree at the ±2σ level, with the exception of C_{33} and C_{66}; indeed, most agree at the ±1σ level. The differences, which are within 1% for most of the elastic moduli, are probably mostly due to differences in composition between the two diopside samples. The sensitivity of C_{66} to composition is consistent with previous work on the

enstatite-ferrosilite orthopyroxene solid solution (Bass and Weidner 1984). We also find remarkably good agreement with the results for the chrome-diopside sample studied by Isaak and Ohno (2003), which contained 3% of a hedenbergite component. Results for these three diopside samples generally show a higher degree of internal consistency with each other than with the results of Levien et al. (1979).

Previous work on chrome-diopside reported by Isaak and Ohno (2003) discussed an unusual compositional dependence of the elastic moduli in the jadeite-diopside solid solution series near the diopside end-member. If substantiated, such an unsystematic composition-elasticity relationship would make it difficult to estimate the elastic properties of omphacitic pyroxenes, which are dominant in eclogitic mantle rocks. Clarifying the diopside-jadeite elasticity-composition relations was in fact one of the prime motivations of the present work.

Although there are slight differences in the compositions between the two diopside samples we studied, no great differences in the elastic, bulk, or shear moduli were observed. A similar observation has been made in orthopyroxenes, where incorporation of a modest amount of Ca in the enstatite structure does not greatly affect its elastic properties (Perrillat et al. 2007).

The largest differences between the results of Isaak and Ohno (2003) and Levien (1979) were in the moduli C_{66}, C_{13} and C_{15} (Table 1.2). Isaak and Ohno concluded that if those differences are due to compositional variations, then these elastic moduli must be very sensitive

to small amounts of Na and/or Cr. The two diopside samples from the present study contain no Cr and negligible Na, yet are highly consistent with the results of Isaak and Ohno (2003). Thus, minor compositional variations for near end-member diopside do not have a significant effect on elastic properties. For major variations in composition along the Di-Jd join, our results on diopside suggest a simple, perhaps linear, trend between the moduli C_{66} and C_{15} and composition (Figure 1.2). The one possible exception is C_{13}. The results of this study and those of Isaak and Ohno (2003) suggest that C_{13} is relatively constant with composition, whereas the results of Levien (1979), Collins and Brown (1998) and, to a lesser degree, Bhagat et al. (1992), indicate that C_{13} increases with diopside content. Further studies of intermediate composition omphacites may resolve this one remaining discrepancy in the elasticity of omphacitic pyroxenes.

Our results for the bulk modulus, K_s, are intermediate between those of Levien et al. (1979) and Isaak and Ohno (2003), but there is no statistically significant difference among all these results for K_s. However, the results from this study and from Isaak and Ohno (2003) both suggest that the shear modulus, G, for diopside is 8-10% higher than reported by Levien et al. (1979). Consistent with the results by Isaak and Ohno (2003), we do not observe any effect of small compositional variations on G near the diopside end-member. It seems there are problems with a few of the C_{ij} values reported by Levien et al. (1979).

1.5. Conclusion

We have determined the elastic constants for nearly pure diopside by Brillouin scattering experiments. Our results are in excellent agreement with recent previous work on chrome-diopside investigated using an independent technique (resonant ultrasound spectroscopy, RUS). The present experimental results suggest that the variation of most elastic moduli with composition for clinopyroxenes in the diopside-jadeite system follow simple systematic trends.

References

Bass, J.D. (1989) Elasticity of grossular and spessartite garnets by Brillouin spectroscopy. Journal of Geophysical Research , 94, 7621-7628.

Bass, J.D. and Weidner, D.J. (1984) Elasticity of single-crystal orthoferrosilite. Journal of Geophysical Research, 89, 4359-4371.

Bhagat, S.S., Bass, J.D., and Smyth, J.R. (1992) Single-crystal elastic properties of omphacite-C2/c by Brillouin spectroscopy. Journal of Geophysical Research, 97, 6843-6848.

Collins, M.D. and Brown, J.M. (1998) Elasticity of an upper mantle clinopyroxene. Physics and Chemistry of Minerals, 26, 7-13.

Comodi, P., Princivalle, F., Tirone, M., and Zanazzi, P.F. (1995) Comparative compressibility of clinopyroxenes from mantle nodules. European Journal of Mineralogy, 7, 141-149.

Isaak, D.G. and Ohno, I. (2003) Elastic constants of chrome-diopside: application of resonant ultrasound spectroscopy to monoclinic single-crystals. Physics and Chemistry of Minerals, 30, 430-439.

Kandelin, J. and Weidner, D.J. (1988a) Elastic properties of hedenbergite. Journal of Geophysical Research, 93, 1063-1072.

Kandelin, J. and Weidner, D.J. (1988b) The single-crystal elastic properties of jadeite. Physics of the Earth and Planetary Interiors, 50, 251-260.

Levien, L. and Prewitt, C.T. (1981) High-pressure structural study of diopside. American Mineralogist, 66, 315-323.

Levien, L., Weidner, D.J., and Prewitt, C.T (1979) Elasticity of diopside. Physics and Chemistry of Minerals, 4, 105-113.

McDonough, W.F. (1990) Constraints on the composition of the continental lithospheric mantle. Earth and Planetary Science Letters, 101, 1-18.

Norris, S. and Bass, J.D. (2010) Sound velocities and elastic properties of single-crystal jadeite. In preparation.

Perrillat, J.-P., Nestola, F., Sinogeikin, S.V., and Bass, J.D. (2007) Single-crystal elastic properties of $Ca_{0.07}Mg_{1.93}Si_2O_6$ orthopyroxene. American Mineralogist, 92, 109-113.

Sinogeikin, S.V., Katsura, T., and Bass, J.D. (1998) Sound velocities and elastic properties of Fe-bearing wadsleyite and ringwoodite. Journal of Geophysical Research, 103, 20819-20825.

Watt, J.P., Davies, G.F., and O'Connell, R.J. (1976) Elastic Properties of Composite-Materials. Reviews of Geophysics and Space Physics, 14, 541-563.

Warren, B.E. and Bragg, W.L. (1928) XII. The structure of diopside, $CaMgSi_2O_6$. Zeitschrift fur Kristallographie, 69, 168-193.

Weidner, D.J. and Carleton, H.R. (1977) Elasticity of coesite. Journal of Geophysical Research, 82, 1334-1346.

Zhang, L. and Hafner, S.S. (1992) High pressure ^{57}Fe gamma resonance and compressibility of $Ca(Fe,Mg)Si_2O_6$ clinopyroxenes. American Mineralogist, 77, 462-473.

Zhang, L., Ahsbahs, H., Turk, P.G., and Hafner, S.S. (1989) A pressure induced phase transition in pyroxene. High Pressure Research, 5, 733-735.

Tables

Table 1.1.

Chemical composition of diopside as compared to chrome-diopside from previous work

Element	Diopside 1*	Diopside 2*	Chrome-diopside†
SiO_2	55.4(3)	53.6(3)	56.1(2)
CaO	26.1(1)	25.4(1)	24.93(9)
Na_2O	0.03(2)	/	0.37(4)
K_2O	/	/	0.004(6)
MgO	18.6(1)	17.8(1)	17.39(8)
Fe_2O_3	0.14(1)	0.79(4)	1.1(1)
Cr_2O_3	/	/	0.84(6)
Al_2O_3	0.05(1)	0.56(2)	0.22(3)
TiO_2	0.03(1)	/	0.07(1)
MnO	0.02(2)	0.06(1)	0.05(5)
Total	100.37	98.11	101.1

*This work. Numbers in parentheses are the standard deviation of measurements from 9 spots for diopside 1 and 3 spots for diopside 2.

†Isaak and Ohno (2003). Numbers in parentheses are the standard deviation of measurements from five spots.

Table 1.2.

Single-crystal elastic moduli (GPa) of diopside for this work in comparison to previous work.

Elastic Constants	Diopside 1*	Diopside 2*	Chrome-diopside†	Diopside‡
C_{11}	229.0(4)	226.1(9)	228.1(10)	223(2)
C_{22}	179.0(4)	179.5(8)	181.1(6)	171(2)
C_{33}	242.5(4)	239.2(9)	245.4(13)	235(2)
C_{44}	78.9(3)	78.1(6)	78.9(3)	74(1)
C_{55}	68.1(2)	69.2(4)	68.2(2)	67(1)
C_{66}	78.2(3)	76.4(8)	78.1(2)	66(2)
C_{12}	78.0(7)	77.4(10)	78.8(5)	77(3)
C_{13}	69.8(6)	70.2(13)	70.2(7)	81(2)
C_{23}	58.0(7)	56.7(16)	61.1(7)	57(2)
C_{15}	9.9(3)	9.9(7)	7.9(5)	17(1)
C_{25}	6.1(5)	5.9(12)	5.9(5)	7(2)
C_{35}	40.9(3)	41.0(7)	39.7(4)	43(1)
C_{46}	6.6(2)	6.8(4)	6.4(2)	7.3(9)
K_s	114.6(7)	113.7(8)	116.5(9)	113(4)
G	72.7(4)	72.2(5)	72.8(4)	67(2)

*This work. Numbers in parentheses are ±1σ based on RMS error of 20 m/s (diopside 1) and 26 m/s (diopside 2). Hashin-Shtrikman bounds are considered in the uncertainties of K_s and G.

† Isaak and Ohno (2003). Uncertainties in C_{ij} mainly come from the standard deviations of the fitted frequencies. Hashin-Shtrikman bounds are considered in the uncertainties of K_s and G.

‡ Levien et al. (1979). Numbers in parentheses are ±1σ based on RMS error of 102 m/s. Voigt-Reuss bounds are considered in the uncertainties of K_s and G.

Figures

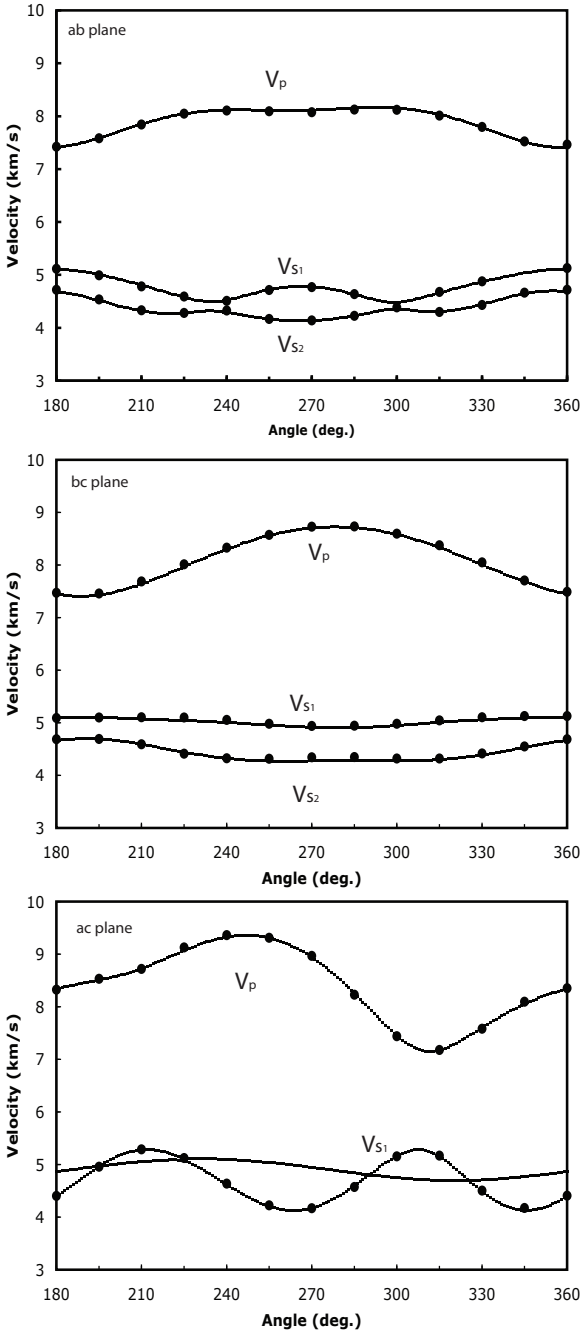

Figure 1.1. Measured acoustic velocities as a function of orientation on the sample surface (expressed as azimuthal angle with respect to an arbitrary direction) for diopside at ambient conditions. The velocities within three orthogonal principal planes are shown.

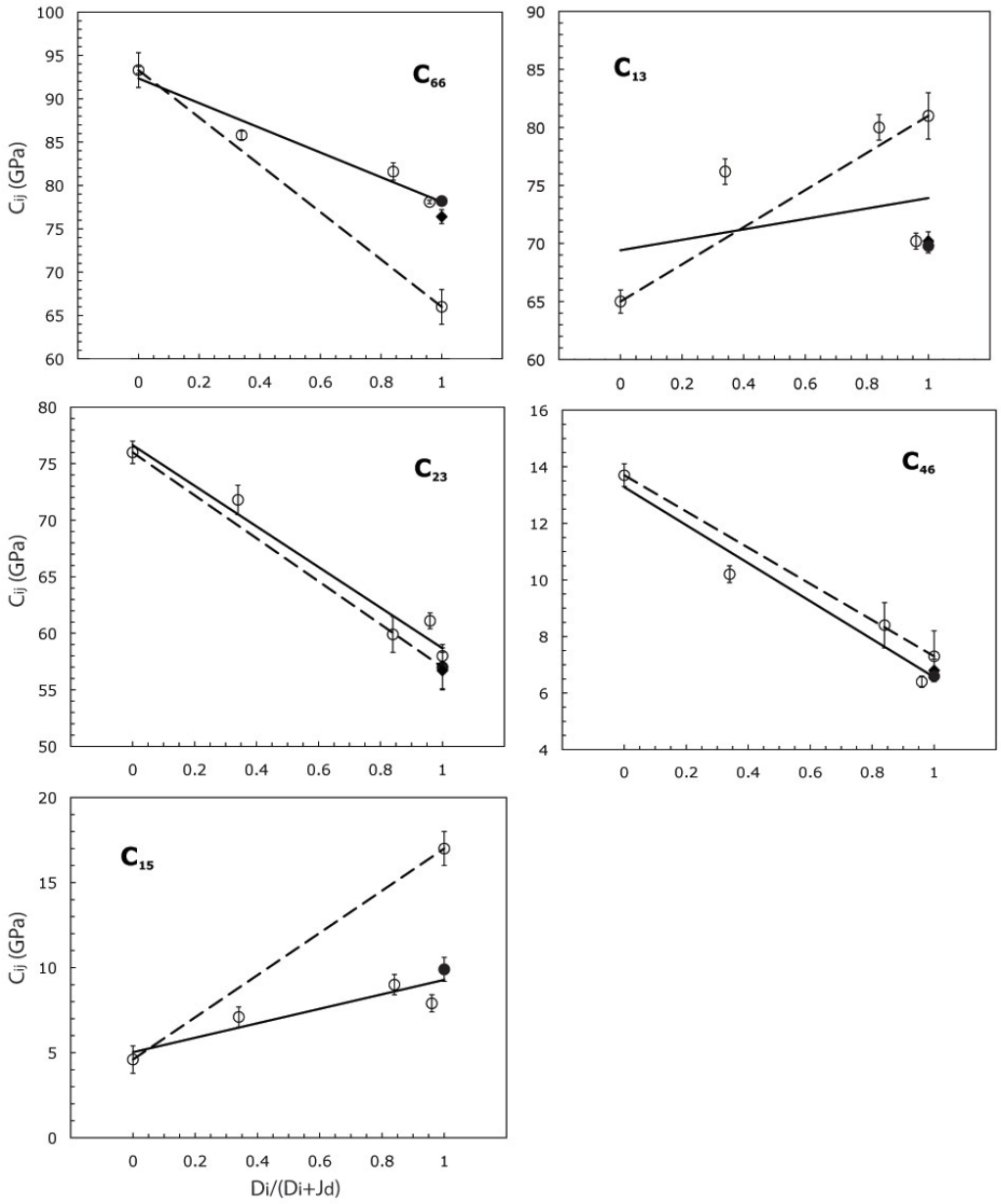

Figure 1.2. The variation of C_{66}, C_{13}, C_{23}, C_{46} and C_{15} with composition in the diopside-jadeite system. For results near Di/(Di+Jd)=1.0, open circles are from Levien et al (1979), solid circles are diopside #1 of this study, and solid diamonds are diopside #2 of this study. Open circles indicate data at nominal Di/(Di+Jd) ratios of 0.0 (Norris and Bass, 2010); 0.34 (Bhagat et al. 1992); 0.84 (Collins and Brown 1998); and 0.96 (Isaak and Ohno 2003). The solid lines show linear fits using the results of the present study for end-member diopside, excluding the results of Levien et al. (1979). The dashed lines simply connect the data for Jd and the results of Levien et al. (1979).

Chapter 2

The elastic properties of diopside up to 14 GPa

Abstract

The single-crystal elastic constants (C_{ij}) of diopside have been measured up to 14 GPa using Brillouin spectroscopy, from which the aggregate compressional and shear velocities, adiabatic bulk modulus, shear modulus and their pressure derivatives were obtained. The best fit of the velocity-pressure data to third-order finite strain equation gives K'_s = 4.8(2) GPa, G' = 1.7(1) GPa with ρ_0 = 3.264(6) g/cm^3, K_s = 114.6(7) GPa and G = 72.7(4) GPa. The current study not only provides the first high-pressure experimental data on the individual C_{ij}'s but also extends direct measurements on shear modulus for diopside to higher pressure than previous studies.

2.1. Introduction

Ca-rich clinopyroxene is considered to be one of the major mineral phases in the Earth's upper mantle and has been an important constituent in various Earth compositional models (Anderson and Bass 1984; Ringwood 1970). In order to interpret seismologically determined models of upper mantle velocity structure and to place constrains on the composition of the

Earth's mantle, accurate values of the elastic properties of mantle minerals and their variation with pressure and temperature is necessary.

The monoclinic mineral diopside ($CaMgSi_2O_6$) is the calcium end member of mantle clinopyroxenes. Its elastic properties at high pressure and temperature (high *P*-*T*) conditions have been a subject several previous studies. The bulk modulus has been measured via several isothermal compression studies using X-ray diffraction (e.g. Levien and Prewitt 1981; Thompson and Downs 2008; Tribaudino et al. 2000; Zhang et al. 1997; Zhao et al. 1998). The adiabatic bulk and shear moduli at high P-T conditions were studied up to 8.4 GPa and 1073K using ultrasonic interferometry and X-ray diffraction (Li and Neuville 2010), and to 1300 K at ambient pressure using resonance ultrasonic spectroscopy (RUS) (Isaak and Ohno 2003; Isaak et al. 2006). The single-crystal elastic moduli (C_{ij}) for near-end-member diopsdie at ambient condition have been measured by Levien et al. (1979) and Sang et al. (2011) using Brillouin spectroscopy, and by Isaak and Ohno (2003) using the RUS method. However, values of the C_{ij}'s at high pressure, which are important for understanding the nature of upper mantle velocity anisotropy, are limited to theoretical simulations by Matsui and Busing (1984) and Walker (2012).

In this study, we report Brillouin scattering measurents of the acoustic velocities of single-crystal diopside in various crystallographic directions up to 14 GPa at ambient temperature, from which the single-crystal elastic moduli, aggregate compressional (V_p) and

shear velocities (V_s), adiabatic bulk modulus (K_s), shear modulus (G) and their pressure dependence were determined.

2.2. Experimental Methods

The single crystals of diopside used in this study were the same samples as the "diopside 1", from Wakefield, Quebec, that were used in previous experiments at ambient conditions (Sang et al., 2011). They are nearly pure end-member diopside samples and the chemical composition is given in Table 1 of Sang et al. (2011). The unit cell volume and density of the samples are 440.7(8) $Å^3$ and 3.264(6) g/cm^3, respectively, as measured by single-crystal X-ray diffractometry. For Brillouin measurements, we prepared three 25-40 μm thick crystals with flat polished surfaces nearly parallel to *a*-*b*, *b*-*c* and *a*-*c* planes. The crystals were oriented by a four-circle X-ray diffractometer. The face normal of the polished surfaces have direction cosines of (0.28686, 0.04260, 0.95703), (0.99959, -0.01640, 0.02355) and (0.03560, 0.99924, -0.01585). For all three polished crystals, the opposite surfaces are parallel to within 0.5º. The polished crystals were then cut into several pieces of desired size for ambient and high-pressure measurments. More details about this diopside sample and sample preparation could be found in Sang et al. (2011).

Two types of diamond-anvil cells (DAC's) were used in the high-pressure experiments: Merrill-Bassett style 3-screw cells, (90º conical opening; Merrill and Bassett, 1974) and 4-screw

piston-cylinder type diamond cells (60º conical opening). Stainless steel gasket were preindented to 50 ~ 70 μm thick and holes with diameters of 185 ~ 235 μm were machined using a micro electric discharge system to form sample chambers. Depending upon the experimental pressure ranges, both neon and a mixture of methanol-ethanol-water (MEW, 16:3:1 by volume) were used as pressure-transmitting media. Several ruby spheres were placed around the sample and experimental pressures were calculated from the ruby fluorescence R1 shift (Mao et al. 1978). Pressure was checked both before and after Brillouin measurements and the difference was within their mutual uncertainties.

An argon ion laser (λ = 514.5 nm) was used as a light source, and the Brillouin measurements were performed using either 50º or 80º symmetric scattering geometry. A six-pass Fabry-Perot interferometer was used to analyze the scattered light for the Brillouin scattered components (Bass 1989; Sinogeikin et al. 1998).

2.3. Results and Discussions

Brillouin measurements were performed at ambient temperature and 8 different pressure points, including the one at 1-atm data. At each pressure point, Brillouin spectra were collected over an angular range of 180º spaced 15º apart in the sample plane. The Brillouin peaks were generally of very good quality with a high signal-to-noise ratio and clearly separated peaks,

except for a few cases where the compressional velocity of the MEW mixture overlapped with the shear velocity of the sample. This overlap occurred for measurements on the (100) and (001) samples at 4.4 GPa. Therefore, neon was used as pressure-transmitting medium instead at this pressure to avoid obscuring the diopside shear waves.

Diopside has monoclinic symmetry with space group *C2/c*. It thus has 13 independent single-crystal elastic moduli that completely characterize its elastic properties. The 13 C_{ij}'s and density of diopside at each pressure were calculated from measured sound velocities in difference phonon directions using the procedure outlined by Sinogeikin and Bass (2000), where a linearized least-squares inversion method was applied (Weidner and Carleton 1977). Briefly, at each pressure, the C_{ij}'s were first solved using an initial set of density values. The aggregate sound velocities (V_p and V_s), which are independent of density, were then calculated using the initial solution for the C_{ij}'s. The obtained aggregate velocity-pressure data, ρ_0, and the finite strain equation of Davies and Dziewonski (1975) were used to determine the pressure derivatives of the aggregate elastic moduli. Finally, the density as a function of pressure was calculated through integration of the bulk modulus. The C_{ij} and aggregate elastic moduli (Table 2.1, Figure 2.1) at each pressure were then re-determined using the revised density values. This procedure was iteratively applied until convergence was obtained for the C_{ij}'s and density at high pressure. The elastic properties of diopside (Figure 2.1) were found to display a linear dependence on

pressure within the uncertainties. The Hill average of the Voigt and Reuss bounds (VRH) was used for all the calculation of aggregate elastic properties. The average of the Voigt and Reuss bounds, which give the aggregate bulk and shear moduli (K_S and G), are consistent with the arithmetic means of the Hashin-Shtrikman bounds (Watt 1980). The latter will narrow the uncertainty from the VRH considerably. Both the width of the Hashin-Shtrikman bounds and statistical uncertainties of individual C_{ij}'s were considered in the errors of K_S and G (Watt et al. 1976). The former was found to dominate the uncertainties of elastic moduli at ambient pressure while the latter was dominant for high-pressure data.

The aggregate velocities were fitted to third-order finite-strain equation of state (Davies and Dziewonski, 1975), yielding best-fit values of the aggregate elastic moduli and their pressure derivatives of: K'_S = 4.8(2) GPa, G' = 1.7(1) GPa with ρ_0 = 3.264(6) g/cm^3, K_S = 114.6(7) GPa and G = 72.7(4) GPa (Table 2.2) (where primes indicate the pressure derivatives of elastic moduli).

Figure 2.2 shows a comparison between the normalized volume (V/V_0) calculated from our Brillouin results and compression measurements from X-ray diffraction studies. The compression curve from current study is seen to be in excellent agreements with the aggregate static compression data within 0.3%. This suggests that Brillouin spectroscopy and other acoustic methods provide an effective means of determining the density of minerals at high pressure, with

accuracy comparable to static-compression X-ray diffraction measurements (Sinogeikin and Bass 2000).

A comparison of the values of K_s, G, V_p, V_s and their pressure derivatives calculated from our Brillouin measurements, with those from a recent ultrasonic study on polycrystalline samples by Li and Neuville (2010), show remarkably good agreements (Figure 2.1 and Table 2.1). This is actually one of the best examples where Brillouin and ultrasonic study give very consistent results on elastic properties of minerals. Previous Brillouin study on MgO (periclase) and $MgSiO_3$ perovskite yield significant lower values (by ~20%) of zero-pressure G' (Murakami et al. 2007; Murakami et al. 2009). However, the values of isothermal bulk modulus and its pressure derivative for diopside, as obtained from different static-compression X-ray diffraction measurements, exhibit a very broad range with differences of ranging from 10% in K and 60% in K'. These discrepancies could be partially due to the trade-off among K, K' and V_0 in the equation of state fit to the experimentally derived pressure-volume relationship from X-ray diffraction studies (Li and Neuville 2010). As discussed above and shown in Figure 2.2, the differences among independent compression curves is less than 0.5% and cannot account for the discrepancy observed in bulk modulus and its pressure derivative. A detailed comparison of individual C_{ij}, bulk and shear moduli and their compositional dependence as inferred from different acoustic studies performed under ambient condition, can be found in Sang et al. (2011).

Determinations of the single-crystal elastic moduli of diopside at high pressure have thus far been limited to theoretical simulations (Matsui and Busing 1984; Walker 2012). To our knowledge, the results reported here are the first experimentally determined values of the C_{ij}'s (Table 2.1 and Figure 2.3). Figure 2.3 shows a comparison between our results on the pressure dependence of individual C_{ij} and those from Walker (2012). The shear moduli C_{55} and C_{66} from the two studies are in good agreement up to 15 GPa. For the longitudinal moduli C_{22} and C_{33} Walker (2012) obtained lower values than those obtained in this study at pressure higher than 10 GPa, with differences of 7% and 6% respectively, at 20 GPa. Walker reported systematically larger values for C_{11}, C_{12}, C_{13}, C_{23}, C_{25} and C_{35}, with difference up to 24%, but lower values for C_{44}, C_{15} and C_{46}. The uncertainty of C_{ij}'s for both studies is typically less than 2 GPa, which can not resolve the discrepancies discussed above. In both studies negative pressure derivatives were obtained for C_{15}, C_{25}, C_{35} and C_{46}. It's worth noting that the pressure derivative of C_{ij} (C_{ij}') from these two studies are generally in broad agreement, with the exceptions of C_{11}, C_{22} and C_{33}, where Walker (2012) obtained lower values. With some of the calculated values being lower than our measurements, while others being higher, there is perhaps fortuitously good agreement between the values of K' (4.7 from Walker (2012) and 4.8 from this study).

2.4. Conclusion

We have determined the single-crystal elastic constants for end-member diopside by Brillouin spectroscopy up to 14 GPa at ambient temperature. The derived aggregate elastic properties, V_p, V_s, K_s, G, K_s' and G', are in excellent agreement with recent previous work on polycrystalline diopside using a combined ultrasonic interferometry and X-ray diffraction methods. Discrepancies between the present measurements and recent values from theoretical calculations of the C_{ij} values at high pressure remain to be reconciled by further investigations.

References

Anderson, D.L., and Bass, J.D. (1984) Mineralogy and composition of the upper mantle. Geophysical Research Letters, 11(7), 637-640.

Bass, J.D. (1989) Elasticity of grossular and spessartite garnets by brillouin spectroscopy. Journal of Geophysical Research-Solid Earth and Planets, 94(B6), 7621-7628.

Davies, G.F., and Dziewonski, A.M. (1975) Homogeneity and constitution of earths lower mantle and outer core. Physics of the Earth and Planetary Interiors, 10(4), 336-343.

Isaak, D.G., and Ohno, I. (2003) Elastic constants of chrome-diopside: application of resonant ultrasound spectroscopy to monoclinic single-crystals. Physics and Chemistry of Minerals, 30(7), 430-439.

Isaak, D.G., Ohno, I., and Lee, P.C. (2006) The elastic constants of monoclinic single-crystal chrome-diopside to 1,300 K. Physics and Chemistry of Minerals, 32(10), 691-699.

Levien, L., and Prewitt, C.T. (1981) High-pressure structural study of diopside. American Mineralogist, 66(3-4), 315-323.

Levien, L., Weidner, D.J., and Prewitt, C.T. (1979) Elasticity of diopside. Physics and Chemistry of Minerals, 4(2), 105-113.

Li, B.S., and Neuville, D.R. (2010) Elasticity of diopside to 8 GPa and 1073 K and implications for the upper mantle. Physics of the Earth and Planetary Interiors, 183(3-4), 398-403.

Liebermann, R.C., and Mayson, D.J. (1976) Elastic properties of polycrystalline diopside ($CaMgSi_2O_6$). Physics of the Earth and Planetary Interiors, 11(3), P1-P4.

Mao, H.K., Bell, P.M., Shaner, J.W., and Steinberg, D.J. (1978) Specific volume measurements of Cu, Mo, Pd, and Ag and calibration of ruby R1 fluorescence pressure gauge from 0.06 to 1 Mbar. Journal of Applied Physics, 49(6), 3276-3283.

Matsui, M., and Busing, W.R. (1984) Calculation of the elastic-constants and high-pressure properties of diopside, $CaMgSi_2O_6$. American Mineralogist, 69(11-1), 1090-1095.

Merrill, L., and Bassett, W.A. (1974) Miniature diamond anvil pressure cell for single-crystal X-ray-diffraction studies. Review of Scientific Instruments, 45(2), 290-294.

Murakami, M., Ohishi, Y., Hirao, N., and Hirose, K. (2009) Elasticity of MgO to 130 GPa: Implications for lower mantle mineralogy. Earth and Planetary Science Letters, 277(1-2), 123-129.

Murakami, M., Sinogeikin, S.V., Hellwig, H., Bass, J.D., and Li, J. (2007) Sound velocity of MgSiO3 perovskite to Mbar pressure. Earth and Planetary Science Letters, 256(1-2), 47-54.

Ringwood, A.E. (1970) Phase transformations and the constitution of the mantle. Physics of the Earth and Planetary Interiors, 3, 109-155.

Sang, L.Q., Vanpeteghem, C.B., Sinogeikin, S.V., and Bass, J.D. (2011) The elastic properties of diopside, CaMgSi2O6. American Mineralogist, 96(1), 224-227.

Sinogeikin, S.V., and Bass, J.D. (2000) Single-crystal elasticity of pyrope and MgO to 20 GPa by Brillouin scattering in the diamond cell. Physics of the Earth and Planetary Interiors, 120(1-2), 43-62.

Sinogeikin, S.V., Katsura, T., and Bass, J.D. (1998) Sound velocities and elastic properties of Fe-bearing wadsleyite and ringwoodite. Journal of Geophysical Research-Solid Earth, 103(B9), 20819-20825.

Thompson, R.M., and Downs, R.T. (2008) The crystal structure of diopside at pressure to 10 GPa. American Mineralogist, 93(1), 177-186.

Tribaudino, M., Prencipe, M., Bruno, M., and Levy, D. (2000) High-pressure behaviour of Ca-rich C2/c clinopyroxenes along the join diopside-enstatite ($CaMgSi_2O_6$-$Mg_2Si_2O_6$). Physics and Chemistry of Minerals, 27(9), 656-664.

Walker, A.M. (2012) The effect of pressure on the elastic properties and seismic anisotropy of diopside and jadeite from atomic scale simulation. Physics of the Earth and Planetary Interiors, 192, 81-89.

Watt, J.P. (1980) Hashin-Shtrikman bounds on the effective elastic-moduli of polycrystals with monoclinic symmetry. Journal of Applied Physics, 51(3), 1520-1524.

Watt, J.P., Davies, G.F., and Oconnell, R.J. (1976) Elastic properties of composite-materials. Reviews of Geophysics, 14(4), 541-563.

Weidner, D.J., and Carleton, H.R. (1977) Elasticity of coesite. Journal of Geophysical Research, 82(8), 1334-1346.

Zhang, L., Ahsbahs, H., Hafner, S.S., and Kutoglu, A. (1997) Single-crystal compression and crystal structure of clinopyroxene up to 10 GPa. American Mineralogist, 82(3-4), 245-258.

Zhao, Y., Von Dreele, R.B., and Weidner, D.J. (1998) Thermoelastic equation of state of monoclinic pyroxene: $CaMgSi_2O_6$ diopside. Review of High Pressure Science and Technology, 7, 25-27.

Tables

Table 2.1. Single-crystal and aggregate elastic moduli (GPa) of diopside as a function of pressure

	0 GPa	4.5(1) GPa	6.10(9) GPa	7.11(6) GPa	8.9(1) GPa	10.5(3) GPa	12.2(2) GPa	14.0(4) GPa
C_{11}	229.0(4)	258(2)	265(1)	273(1)	284(1)	292(2)	299(1)	310(2)
C_{22}	179.0(4)	209(1)	214(1)	221(1)	230(1)	241(2)	247(1)	254(1)
C_{33}	242.5(4)	276(1)	285(1)	294(1)	301(1)	312(2)	321(1)	331(1)
C_{44}	78.9(3)	83.5(9)	92(1)	90.9(7)	91.8(8)	96(1)	93.0(8)	100(1)
C_{55}	68.1(2)	74.6(9)	79.9(7)	81.1(7)	82.8(6)	85.3(8)	85.1(8)	86.8(8)
C_{66}	78.2(3)	82(1)	90(1)	93.1(8)	98(1)	102(1)	104(1)	106(1)
C_{12}	78(7)	97(2)	100(2)	108(2)	113(2)	116(2)	127(2)	121(3)
C_{13}	69.8(6)	89(3)	93(2)	98(2)	103(2)	111(2)	113(2)	118(2)
C_{23}	58.0(7)	66(2)	74(3)	82(2)	91(2)	86(3)	108(2)	96(3)
C_{15}	9.9(3)	8(1)	7(1)	5.7(8)	5.2(9)	5(1)	5(1)	7(1)
C_{25}	6.1(5)	2(2)	-4(2)	-2(1)	-3(2)	-9(2)	3(2)	-13(2)
C_{35}	40.9(3)	34(1)	34(1)	34.3(9)	31.7(9)	30(1)	29(1)	27(1)
C_{46}	6.6(2)	1(1)	2(1)	1.4(8)	-2(1)	4(1)	1(1)	5.2(8)
K_s (GPa)	114.6(7)	136(1)	142.4(9)	149.5(7)	157.2(8)	162(1)	172.1(8)	173(1)
G (GPa)	72.7(4)	79.4(5)	83.8(5)	84.7(4)	86.7(4)	90.5(5)	89.5(4)	94.2(5)
V_p(km/s)	8.06	8.46	8.61	8.73	8.84	8.95	9.05	9.11
V_s(km/s)	4.72	4.84	4.95	4.96	4.99	5.07	5.01	5.12
ρ(g/cm^3)	3.264	3.385	3.424	3.446	3.489	3.524	3.560	3.597

* Error bars for acoustic velocities are typically less than 63 m/s.

Table 2.2. Elasticity of diopside* in comparison to previous work

References	V_0 (Å^3)	Max P(GPa)	K (GPa)	K'	G (GPa)	G'	Method/sample
This study and Sang et al. (2011)	440.7(8)	14	114.6(7)	4.8(2)	72.7(4)	1.7(1)	BS/single
Li and Neuville (2010)	439.13(4)	8	116.4(7)	4.9(1)	73.0(4)	1.6(1)	UI + X-ray/poly
Levien and Prewitt (1981)[a]	439.13(6)	5.3	113(3)	4.7(7)			X-ray/single
Tribaudino et al. (2000)[a]	439.465(16)	40.8	105.1(9)	6.8(1)			X-ray/poly
Zhang et al. (1997)[a]	438.82(11)	10	104.1(9)	6.2(3)			X-ray/single
Thompson and Downs (2008)[a]	438.66(2)	10	118(1)	3.8(2)			X-ray/single
Matsui and Busing (1984)		5	105	6.2			Theory
Walker et al. (2008)[a]	439.1	25	122.0	4.7			Theory
Liebermann and Mayson (1976)		0.75	113		74.6		UI/poly
Levien et al. (1979)		0	113		67		BS/single
Isaak et al. (2006, $Di_{93}Hd_3Ur_2X_2$)		0	116.5(9)		72.8(4)		RUS/single

UI, ultrasonic interferometry; RUS, resonance ultrasonic spectroscopy; poly, polycrystalline sample; single, single crystal.

* The results are for end-member diopside unless noted.

[a] Isothermal value. Elastic moduli are adiabatic values unless noted, $K_S/K_T \sim 1.008$ for diopside.

Figures

Figure 2.1. (a)

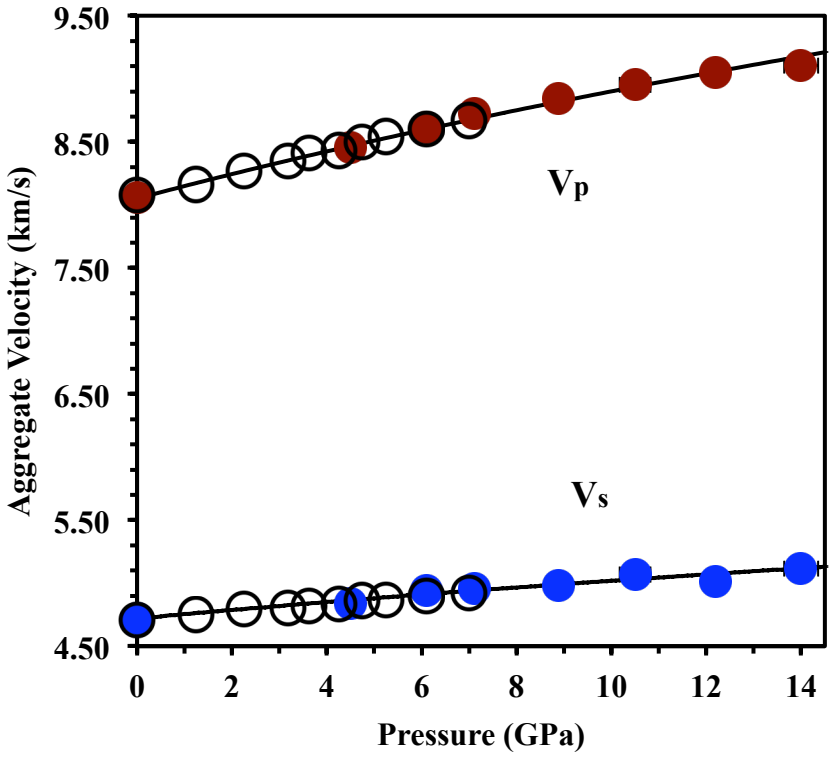

Figure 2.1. (b)

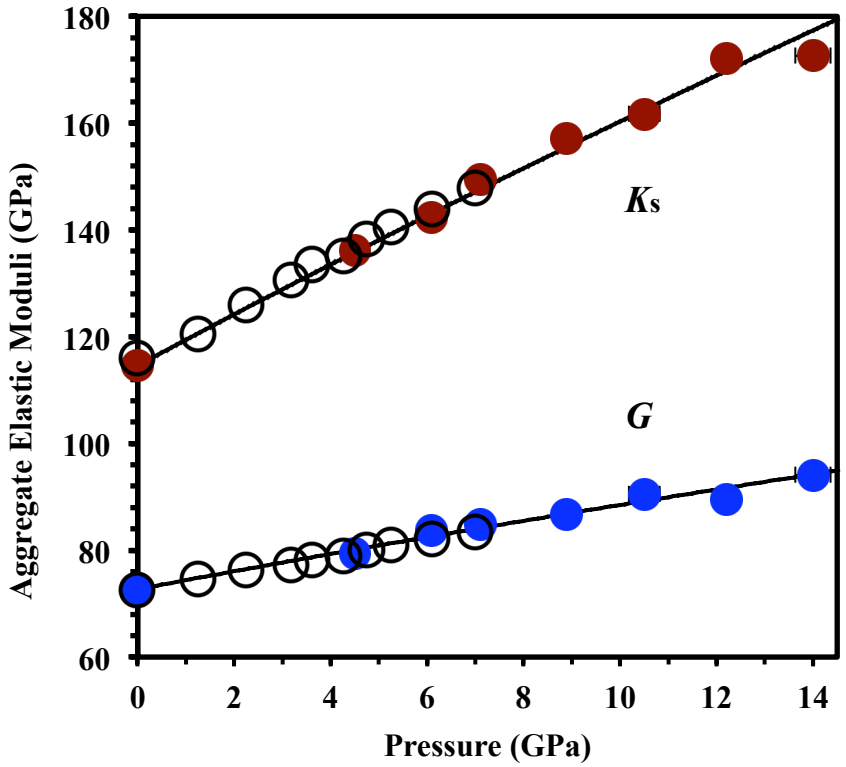

Figure 2.1. (a) Aggregate acoustic velocities and (b) aggregate elastic moduli in diopside as a function of pressure. Solid and open symbols represent experimental data from this study and Li and Neuville (2010), respectively. Solid lines are calculated from best-fit elastic moduli using third-order finite-strain EOS.

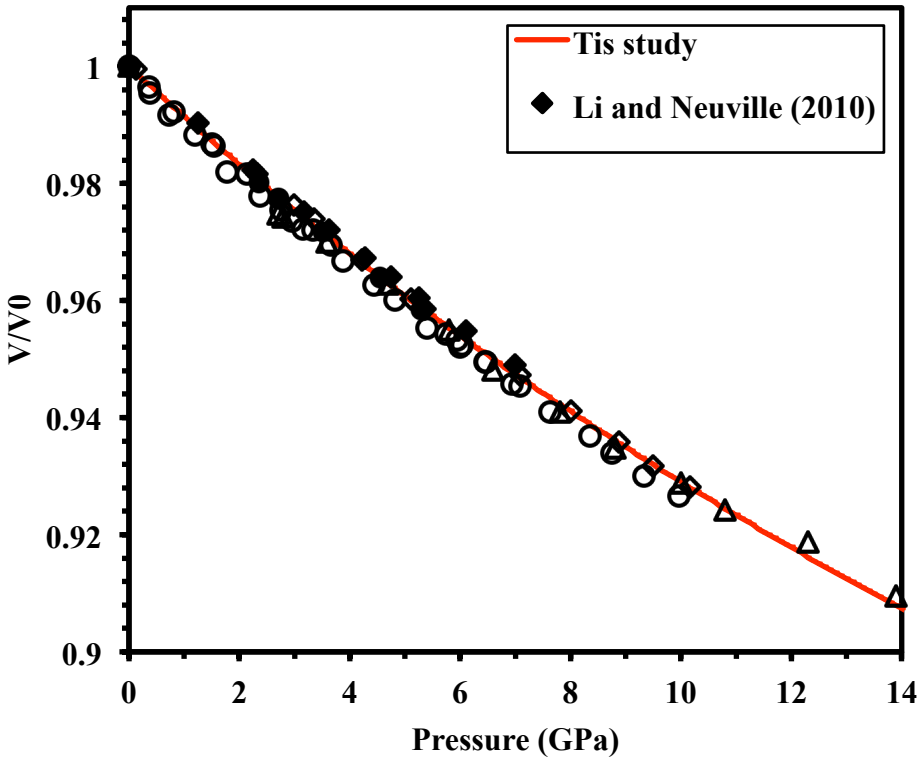

Figure 2.2. Normalized volume (V/V_0) as a function of pressure calculated from Brillouin results in comparison to static compression experiments.

Figure 2.3. (a)

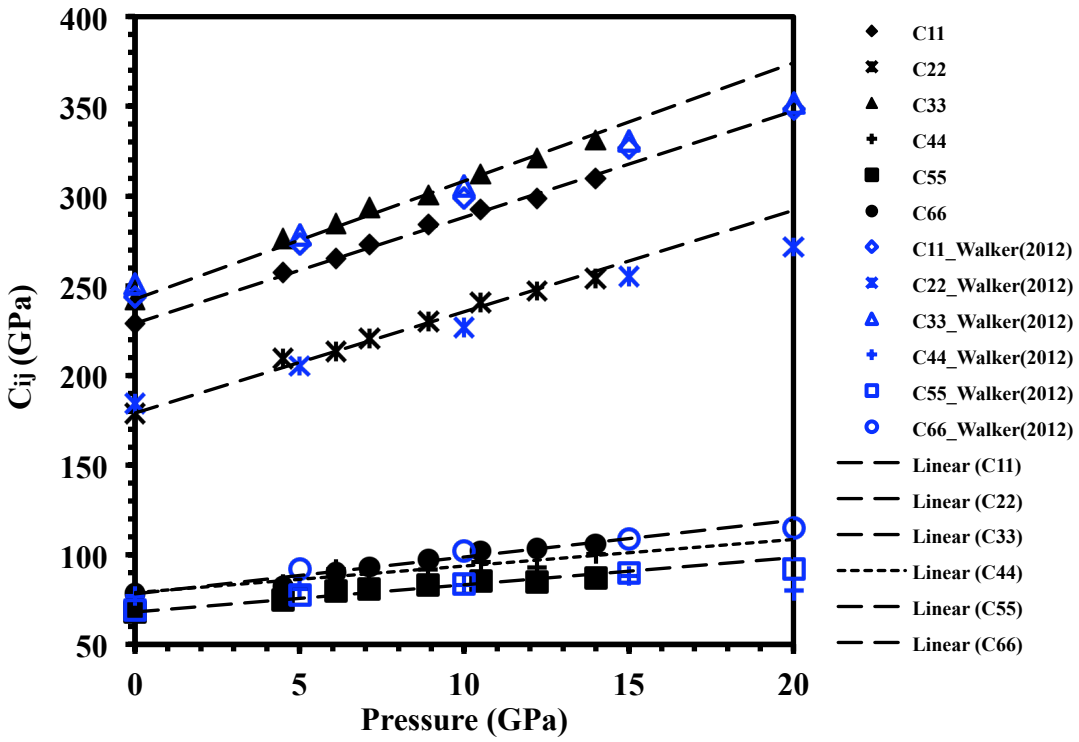
400
350
300
250
200
150
100
50
0
5
10
15
20
Cij (GPa)
Pressure (GPa)
C11
C22
C33
C44
C55
C66
C11_Walker(2012)
C22_Walker(2012)
C33_Walker(2012)
C44_Walker(2012)
C55_Walker(2012)
C66_Walker(2012)
Linear (C11)
Linear (C22)
Linear (C33)
Linear (C44)
Linear (C55)
Linear (C66)

Figure 2.3. (b)

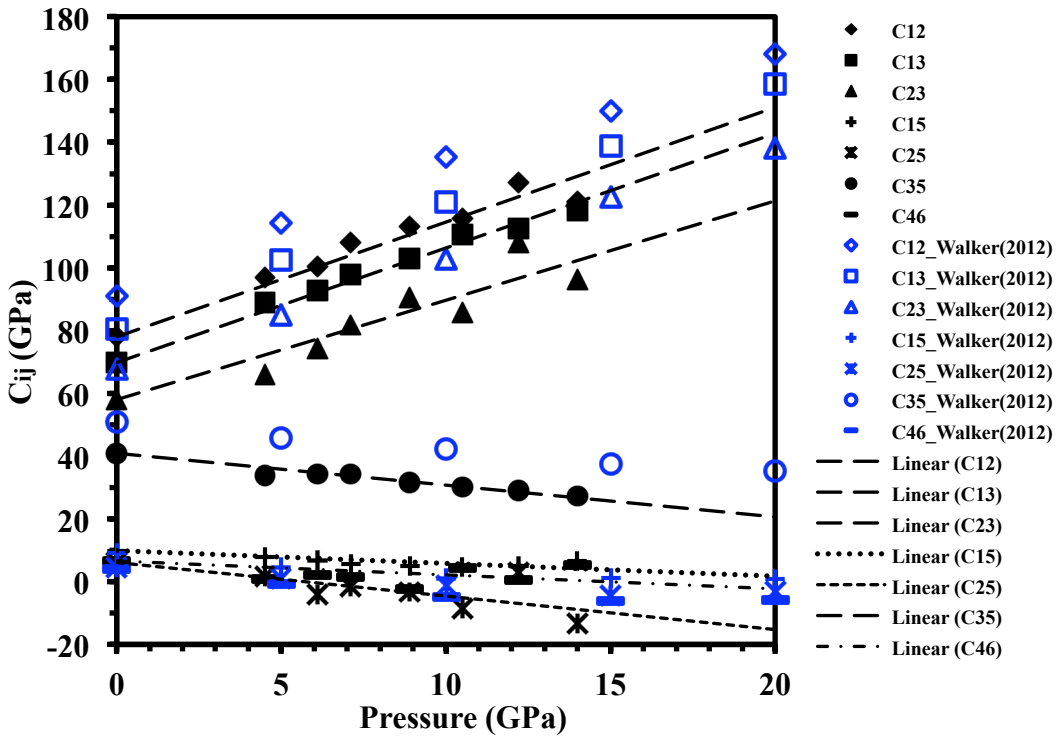

Figure 2.3. Comparison of $C_{ij} - P$ relation for diopside from this study (black symbols) and previous simulation results (Walker 2012, blue symbols). (a) Diagonal elements; (b) off-diagonal elements. Straight lines are the linear fitting curves of the data from this study with C_{ij} values at ambient pressure fixed. Error bars on the C_{ij} and pressure are smaller than the symbol size.

Chapter 3

Melting curve of Ice VII and equation of state of liquid H_2O at high pressure and high temperature

Abstract

We determined the melting curve of Ice VII by simultaneous measurements of sound velocity and angle-dispersive synchrotron x-ray diffraction in a membrane-type diamond anvil cell (DAC) with resistance heating at elevated temperatures to 873 K, and at pressures of 2 GPa to 14 GPa. All our samples were contained within, and chemically insulated from, the Re-gasket hole by a fine gold liner. This Au liner also served as the pressure calibrant through measurments of its lattice parameter and unit cell volume by synchrotron X-ray diffraction. We observed higher melting temperatures than those of Datchi et al. (2000), Dubrovinskaia and Dubrovinsky (2003), and Lin et al. (2004) above 6 GPa, with the differences in melting temperatures of ~120 K at 8 GPa. Given the care taken in the present experiments to avoid potential contamination of the water sample due to reactions at high temperatures between the sample and the gaskets and/or pressure gauges, our new measurements likely provide the first measurements on pure water. This may explain the extended stability field of the solid phase in our experiments. Thus, our

new measurements suggest that the melting curve of H_2O at high pressure needs to be reevaluated using improved experimental techniques.

The sound velocity of liquid H_2O was measured up to 723K and 6.3 GPa. Measured sound speeds are significantly lower than observed in previous acoustic measurements, with discrepancies as high as 9% along 723K isotherm. A tentative equation of state (EOS) for liquid H_2O was obtained with the velocity – pressure – temperature data. More sound velocity data at different pressure along several high-temperature isotherms is required for a more accurate estimate of the EOS.

3.1. Introduction

The physical properties and phase diagram of both Ice VII and liquid water at high pressure and high temperature are of fundamental interest in physics, chemistry and planetary sciences. Ice VII is a stable ice phase at room temperature and pressures from 2 GPa to approximately 60 GPa. Knowledge of its phase diagram is key to understanding many phenomena in the interior of the Earth and large icy planets (Consolmagno and Lewsis, 1976; Anderson et al., 1998; Scott et al., 2002; Bina and Navortsky, 2000). The melting curve of Ice VII has been studied using various types of high-pressure apparatuses, but their results are not consistent (Bridgman, 1937; Pistorius et al., 1963; Mishima and Endo, 1978; Fei et al., 1993;

Datchi et al., 2000; Dubrovinskaia and Dubrovinsky, 2003; Frank et al., 2004; Lin et al., 2004; Schwager et al., 2004). This could be due to the different methods they used to determine melting. On the other hand, if not enough care was taken, the sample can be contaminated through chemical reactions with the sample container material at high temperature which, in the case of diamond-anvil cell experiments, is the gasket material. An additional potential source of chemical contamination is any pressure-sensing material in the sample chamber, such as ruby. The first high-pressure measurements on water and ice were carried out by Bridgman (1937) up to 3.9 GPa using a Bridgman piston-cylinder press. Subsequent studies performed in large-volume presses were those of by Pistorius et al. (1963) and Mishima and Endo (1978), in which melting was inferred from a change in electrical resistance. The results of these studies agree well with those from Fei et al. (1993) and Frank et al. (2004), who used the disappearance of the Ice VII (110) peak in energy-dispersive synchrotron x-ray diffraction measurements. However, Datchi et al. (2000) obtained much higher melting temperatures by visual observations of the Ice VII melting; pressure were determined from the shifts of $SrB_4O_7:Sm^{2+}$ fluorescence lines, and temperature from the ruby R1 shift. Angle-dispersive synchrotron x-ray measurements by Dubrovinskaia and Dubrovinsky (2003) and Raman spectroscopy measurements by Lin et al. (2004) yielded similar melting curves to those of Datchi et al. (2000). The melting curve of Ice VII has also been studied in a laser heated DAC by Schwager et al. (2004), which gave the

highest melting temperatures thus far obtained. Furthermore, the results of these previous studies show large differences in slopes of the melting curve, which can lead to very different predictions for the stability field of Ice VII at higher pressures.

Shock wave experiments have served as the main tool for the derivations of EOS of liquid water (e.g., Rice and Walsh, 1957; Saxena and Fei, 1987; Belonoshko and Saxena, 1991; Pitzer and Sterner, 1994; Sakane et al., 2001). Static high pressure-temperature measurements are needed to test the validity of these models. However, direct measurements on liquid water are very difficult and thus very few studies have been reported. Fei et al. (1993), Fei and Mao (1993) and Frank et al. (2004) used the melting curve of Ice VII to constrain the EOS of liquid water along the melting curve up to 41 GPa. Sound velocity measurements in a diamond-anvil cell have been used to determine the EOS of water under high P-T conditions (Wiryana et al., 1998; Abramson and Brown, 2004; Decremps et al., 2006), extending the equation state of water at temperatures up to 723 K and pressures up to 9 GPa. However, these results do not agree with theory (Wagner and Pruss, 2002), suggesting that at present the potential models used in the simulations may not achieve the accuracy required to usefully predict the thermodynamic properties of water in the upper mantle. On the other hand, supercritical water is very aggressive and tends to react with pressure markers and/or gasket materials (Wiryana et al., 1998; Decremps et al., 2006), which could result in misleading measurements that do not represent the properties

of pure H_2O. This is currently a significant challenge for high P-T experimental studies on liquid water. Recently, measurements of the sound velocity in water were extended to 25 GPa and 900 K by Asahara et al. (2010) using a laser heated DAC with a combined system of Brillouin scattering and synchrotron X-ray diffraction. Using a laser-heating method, a reaction between water and gasket could be prevented because water is generated in a heated spot smaller than the gasket hole, and the surrounding ice serves as a chemical insulator. Asahara et al. (2010) then evaluated the densities of water using Murnaghan's equation of state over a pressure range corresponding to the melting curve of Ice VII.

In this study we measured the melting temperature of Ice VII to 12 GPa and the sound velocities of liquid H_2O up to 723K and 6.3 GPa in a resistance-heated membrane-type DAC with a combined system of Brillouin scattering and synchrotron X-ray diffraction. Melting was determined by monitoring the change in sound velocities, and the disappearance/appearance of the diffraction peaks of Ice VII in angle-dispersive X-ray diffraction measurements. The obtained sound velocity data across a range of pressures and temperatures allow us to develop a tentative EOS of liquid H_2O.

3.2. Experimental Methods

The liquid H_2O sample was loaded into the sample chamber (100~200 μm) of a membrane-type diamond anvil cell. Unlike the more common screw-driven DAC, high pressure inside the sample chamber of a membrane DAC is obtained by applying a gas pressure on a flexible membrane mounted to the DAC. The gas pressure causes the membrane to expand and this inflation provides force to the DAC piston, increasing sample pressure between the diamonds. Therefore a membrane cell offers very fine control over pressure, and the pressure can be increased without removing the cell from the X-ray or Brillouin system. The particular membrane DAC used in our experiments (Antonangeli et al., 2011) also comes with a vacuum chamber, which thermally insulates the DAC from the environment and greatly reduces the heat loss, thus leading to very efficient heating.

One of the major technical challenges when working with high reactive aqueous fluids at high temperature in the DAC is the risk of chemical reactions between sample and gasket materials and/or pressure markers (Wiryana et al., 1998; Decremps et al., 2006). To resolve this problem, we use rhenium gasket with a fine gold liner in the gasket hole to chemically insulate the sample from the gasket (Datchi et al., 2000). The gold liner also serves as a pressure standard in our experiments, in that we use the diffraction peaks of Au to calculate the experimental pressure. We want to avoid using ruby, the most commonly used optical pressure sensor in the

diamond anvil cell (Mao et al., 1978), as our pressure maker for several reasons: Firstly, the broadening and overlapping of ruby lines with increasing temperature will dramatically reduce the accuracy of the pressure measurements; Secondly, ruby can be dissolved by the highly aggressive supercritical water at high temperatures and contaminate our samples. X-ray diffraction patterns of Au were taken from the inner edge of the gold liner, where the H_2O sample and Au have intimate contact. The potential pressure gradient between the center of the sample chamber and the edge was tested to 7 GPa by placing an Au flake inside the sample chamber. We did not observe see any pressure difference between the gold flake and the gold liner despite noticeable stress in some of the Au liner diffraction patterns.

High temperatures were obtained by using a pair of small Mo-wire heaters placed around the diamond anvils. The experimental temperature is determined by placing a type-K thermocouple between each diamond anvil and Re-gasket, directly against the surface of the diamond and as close to the culet as possible. High temperature calibrations on the membrane cells were performed in order to determine the experimental uncertainties of temperature measurement in this study. We put thermocouples in the same position as in our experiments and monitored the melting of several standard melting point materials at atmospheric pressure. These standard materials include NaCl, AgCl and Omega standards, whose melting temperatures are well known. Figure 3.1 shows a comparison of the measured temperature temperatures and

the known melting temperatures of these standard materials at atmospheric pressure. The results show that at temperatures up to 1073K the maximum error in the temperature measurement is ~70 K (Figure 3.1). At lower temperatures the uncertainties in temperature measurement are greatly reduced (<20 K).

We used a combined system of Brillouin scattering and synchrotron X-ray diffraction at the GSECARS 13-BM-D beamline (Sinogeikin et al., 2006) at the Advanced Photon Source, Argonne National Laboratory.

Angle dispersive X-ray diffraction patterns were recorded on a MAR3450 imaging system with a monochromatic focused X-ray beam of 6 μm ×14 μm in size (FWHM). The wavelength of the beam was 0.3344 Å. With the unit cell parameter of Au obtained from the diffraction patterns, experimental pressures were calculated using the Au equation of state of Fei et al. (2007).

A symmetric, or platelet, scattering geometry was used in our Brillouin scattering measurements, with a scattering angle (θ) of 50°. For the platelet geometry, the sound velocity (V) is related to the frequency shift (Δv) of the incident light in a medium by the relation:

$$V = \frac{\lambda_0 \Delta v}{2 \sin(\frac{\theta}{2})}$$

where λ_0 (532.0 nm) is the laser wavelength.

3.3. Results and Discussion

3.3.1. Melting curve of Ice VII

Simultaneous measurements of Brillouin scattering and synchrotron X-ray diffraction on H_2O were performed at P-T conditions up to 14 GPa and 873 K. Data in the vicinity of the melting curve were collected up to 12 GPa and 873 K.

Two source of information was used to determine which phase of H_2O (i.e. Ice VII or liquid water) was present at a given P-T condition: Firstly, the disappearance of Ice VII diffraction lines on heating or the appearance of diffraction lines on cooling in angle-dispersive x-ray diffraction; Secondly there is a large change of sound velocities obtained from Brillouin spectrum (Figure 3.2) for ice VII and water, i.e. the appearance of the compressional mode of Ice VII indicates crystallization. Melting points were approached from different directions, i.e. by increasing temperature with constant load or increasing pressure at constant temperature, to account for any kinetic hindrance of the ice-water transition. Figure 3.3 shows the observed Ice VII and liquid water phase fields, with a fitted melting curve to the following Simon equation (Simon and Glatzel, 1929)

$$\frac{P-2.17}{3.87} = \left(\frac{T}{355}\right)^{1.21} - 1$$

where P is pressure (GPa) and T is temperature (K). P = 2.17 GPa and T = 355 K are used as the Ice VI – VII – liquid triple point. The fit parameters P_C = 3.87 GPa and α =1.21 were obtained

by minimizing the number of P-T points that lie on the wrong side of the melting curve (Lin et al., 2004).

In Figure 3.3, we compare our results to some recent studies on the melting curve of Ice VII using DAC. Generally, we observed higher melting temperatures than those given by previous studies (e.g. Datchi et al., 2000; Dubrovinskaia and Dubrovinsky, 2003; Lin et al., 2004) above 6 GPa, with the discrepancy increasing to ~120 K at 8 GPa. The discrepancy is yet larger when compared to the study of Frank et al. (2004). Frank et al. used the disappearance of Ice VII x-ray diffraction peaks in energy-dispersive experiments to determine the melting. It has been suggested that in energy-dispersive measurements this method can give false melting temperatures because of the recrystallization of Ice VII (Datchi et al., 2000; Lin et al., 2004). Indeed, we observed such recrystallization in some of our angle-dispersive measurements, with the loss of diffraction spots from small crystallites in the powder diffraction patterns. Although it would be difficult to observe this phenomenon in energy-dispersive experiments and angle-dispersive diffraction can't identify all the recrystallization processes because of th area detectors, this is less of an issue in our measurements because we can also use the sound velocity data to as a criterion of melting or crystallization.

Datchi et al. (2000) also used a membrane-type DAC in his study of the ice VII-water boundary. Melting was determined visually and three holes were drilled into a gold liner

isolating the sample from the gasket. Either ruby or $SrB_4O_7:Sm^{2+}$ power was present in each hole. They used the shift in $SrB_4O_7:Sm^{2+}$ line to determine pressure and coupled this value to the ruby R1 shift to determine temperature. However, the ruby R1 shift is strongly influenced by increasing temperature, and both ruby and SrB_4O_7: Sm^{2+} powder readily dissolve in water at high temperature and pressure. All of these effects introduce substantial uncertainties, along with broadening of the ruby and SrB_4O_7: Sm^{2+} fluorescence lines at high temperature. Contamination of the sample from the dissolved ruby or SrB_4O_7: Sm^{2+}, would mean that the measured melting curve is not for the pure H_2O system. Recent Raman measurements by Lin et al. (2004) gave a similar melting curve to that of Datchi et al. (2000). Lin et al. measured temperature from thermocouples in an externally heated DAC and used Sm:YAG as a pressure calibrant. They gave much lower melting temperatures than present study and this could be due to the use of different pressure markers (Au versus Sm:YAG). Dubrovinskaia and Dubrovinsky (2003) determined the melting curve of Ice VII using angle-dispersive x-ray diffraction. They also used Au as the pressure calibrant. But the direct contact between the water sample and Ir gasket in their experiment may have caused contamination of the sample and account for the discrepancy between their results and ours.

3.3.2. EOS of liquid H_2O

Sound velocity data was taken along isotherms of 300, 373, 423, 473, 523 and 723K (Table 3.1, Figure 3.4). In Figure 3.4 we also show other experimental results for the 673K isotherm from Abramson and Brown (2004) and the 723K isotherm from Decremps et al. (2006). We observed lower sound velocities than these two studies, with difference up to 9% along 723K isotherm (Figure 3.4). This may partly due to the inconsistency in different pressure standards and temperature measurements. The error of velocity measurements for all three studies is within 1%, therefore it cannot resolve the discrepancy discussed above.

With the measured sound velocities as a function of pressure and temperature, the equations of state can be determined by the recursive integration of the combined equations (e.g. Wiryana et al., 1998; Abramson and Brown, 2004):

$$\left(\frac{\partial \rho}{\partial P}\right)_T = \frac{1}{V^2} + \frac{T\alpha^2}{c_P} \quad (1)$$

$$\left(\frac{\partial c_P}{\partial P}\right)_T = -T\frac{\partial^2 v_{sp}}{\partial T^2} \quad (2)$$

where ρ is the density, V the measured sound velocity, α the volume coefficient of thermal expansion, c_P the specific heat and v_{sp} the specific volume. Solution of these equations proceeds by first integrating Eq. (1), assuming the second term, which gives the correction from an adiabatic to isothermal path, is negligible. The resulting values of density are used to calculate approximations to the temperature derivative of v_{sp}, and to c_P with Eq. (2). These values are

then used in the next integration of Eq. (1), and the process is repeated until convergence is obtained. To solve for the equation of state independently with this method, sound velocity data spanning a range of pressure and temperature is required. While we do have a reasonable dataset along six isotherms (Figure 3.4), it is intrinsically difficult to obtain the second derivative of v_{sp} with respect to *T*, then c_P, at high pressure because the absence of data for liquid H_2O above the crystalization pressure on each isotherm. For example, above 3 GPa, only data for three isotherms is available (Figure 3.4). Therefore in the current study, we estimate the density using Eq. (1), assuming the second term is negligible. The viability of this method was tested with the data from Abramson and Brown (2004). The maximum difference in density between this calculation and theirs is 4.3% at 6.0 GPa and 673K. Figure 3.5 shows the calculated density from the current study using Eq. (1) without the second term. The difference in density between this study and Abramson and Brown (2004) is within 1%.

3.4. Conclusion

We determined the melting curve of Ice VII up to 12 GPa in a resistance-heated membrane-type DAC. Melting was monitored by the disappearance of Ice VII diffraction patterns in angle-dispersive measurements and by the change of sound velocity in Brillouin spectrum. To avoid the chemical reactions between the water sample and gasket

material/pressure marker at high temperature, we used a gold line around the sample chamber as the chemical insulator, which also serves as the pressure calibrant. Generally, we observed higher melting temperature than all previous studies. Given the care taken in the present experiments to avoid potential contamination of the water sample, our new measurements likely provide the first measurements on pure water which displays an extended stability field of the solid phase. Although many other factors could account for the discrepancy, our new measurements provide clear evidence that the melting curve of Ice VII at high pressure needs to be reevaluated using improved experimental techniques.

We also present new results on the measurement of sound velocity of liquid H_2O up to 723K and 6.3 GPa. A tentative EOS is given for these pressure and temperature conditions. To accurately define the EOS with Eq. (a) and (b), more velocity data along different isotherms at pressure >3 GPa is required.

References

Abramson, E.H., and Brown, J.M. (2004) Equation of state of water based on speeds of sound measured in the diamond-anvil cell. Geochimica Et Cosmochimica Acta, 68(8), 1827-1835.

Anderson, J.D., Schubert, G., Jacobson, R.A., Lau, E.L., Moore, W.B., and Sjogren, W.L. (1998) Distribution of rock, metals, and ices in Callisto. Science, 280(5369), 1573-1576.

Antonangeli, D., Siebert, J., Aracne, C.M., Farber, D.L., Bosak, A., Hoesch, M., Krisch, M., Ryerson, F.J., Fiquet, G., and Badro, J. (2011) Spin Crossover in Ferropericlase at High Pressure: A Seismologically Transparent Transition? Science, 331(6013), 64-67.

Asahara, Y., Murakami, M., Ohishi, Y., Hirao, N., and Hirose, K. (2010) Sound velocity measurement in liquid water up to 25 GPa and 900 K: Implications for densities of water at lower mantle conditions. Earth and Planetary Science Letters, 289(3-4), 479-485.

Belonoshko, A., and Saxena, S.K. (1991) A molecular-dynamics study of the pressure-volume-temperature properties of supercritical fluids .1. H_2O. Geochimica Et Cosmochimica Acta, 55(1), 381-387.

Bina, C.R., and Navrotsky, A. (2000) Possible presence of high-pressure ice in cold subducting slabs. Nature, 408(6814), 844-847.

Bridgman, P. W. (1937) The phase diagram of water to 45,000 kg/cm^2, Journal of Chemical Physics, 5(12), 964-966.

Consolmagno, G.J., and Lewis, J.S. (1978) Evolution of icy satellite interiors and surfaces. Icarus, 34(2), 280-293.

Datchi, F., Loubeyre, P., and LeToullec, R. (2000) Extended and accurate determination of the melting curves of argon, helium, ice (H_2O), and hydrogen (H-2). Physical Review B, 61(10), 6535-6546.

Decremps, F., Datchi, F., and Polian, A. (2006) Hypersonic velocity measurement using Brillouin scattering technique. Application to water under high pressure and temperature. Ultrasonics, 44, E1495-E1498.

Dubrovinskaia, N., and Dubrovinsky, L. (2003) Melting curve of water studied in externally heated diamond-anvil cell. High Pressure Research, 23(3), 307-311.

Fei, Y.W., and Mao, H.K. (1993) Static compression of $Mg(OH)_2$ to 78-GPa at high-temperature and constraints on the equation of state of fluid H_2O. Journal of Geophysical Research-Solid Earth, 98(B7), 11875-11884.

Fei, Y.W., Mao, H.K., and Hemley, R.J. (1993) Thermal expansivity, bulk modulus, and melting curve of H_2O-Ice VII to 20 GPa. Journal of Chemical Physics, 99(7), 5369-5373.

Fei, Y.W., Ricolleau, A., Frank, M., Mibe, K., Shen, G.Y., and Prakapenka, V. (2007) Toward an internally consistent pressure scale. Proceedings of the National Academy of Sciences of the United States of America, 104(22), 9182-9186.

Frank, M.R., Fei, Y.W., and Hu, J.Z. (2004) Constraining the equation of state of fluid H_2O to 80 GPa using the melting curve, bulk modulus, and thermal expansivity of Ice VII. Geochimica Et Cosmochimica Acta, 68(13), 2781-2790.

Lin, J.F., Militzer, B., Struzhkin, V.V., Gregoryanz, E., Hemley, R.J., and Mao, H.K. (2004) High pressure-temperature Raman measurements of H_2O melting to 22 GPa and 900 K. Journal of Chemical Physics, 121(17), 8423-8427.

Mao, H.K., Bell, P.M., Shaner, J.W., and Steinberg, D.J. (1978) Specific volume measurements of Cu, Mo, Pd, and Ag and calibration of ruby R1 fluorescence pressure gauge from 0.06

to 1 Mbar. Journal of Applied Physics, 49(6), 3276-3283.

Mishima, O., and Endo, S. (1978) Melting curve of Ice -7. Journal of Chemical Physics, 68(10), 4417-4418.

Pistorius, C.W.F., Pistorius, M.C.F., Blakey, J.P., and Admiraal, L.J. (1963) MELTING CURVE OF ICE VII TO 200 KBAR. Journal of Chemical Physics, 38(3), 600-602.

Pitzer, K.S., and Sterner, S.M. (1994) Equations of state valid continuously from zero to extreme pressures for H_2O and CO_2. Journal of Chemical Physics, 101(4), 3111-3116.

Rice, M.H., and Walsh, J.M. (1957) Equation of state of water to 250 kilobars. Journal of Chemical Physics, 26(4), 824-830.

Sakane, S., Liu, W.B., Doren, D.J., Shock, E.L., and Wood, R.H. (2001) Prediction of the Gibbs energies and an improved equation of state for water at extreme conditions from ab initio energies with classical simulations. Geochimica Et Cosmochimica Acta, 65(21), 4067-4075.

Saxena, S.K., and Fei, Y. (1987) High-pressure and high-temperature fluid fugacities. Geochimica Et Cosmochimica Acta, 51(4), 783-791.

Schwager, B., Chudinovskikh, L., Gavriliuk, A., and Boehler, R. (2004) Melting curve of H_2O to 90 GPa measured in a laser-heated diamond cell. Journal of Physics-Condensed Matter, 16(14), S1177-S1179.

Scott, H.P., Williams, Q., and Ryerson, F.J. (2002) Experimental constraints on the chemical evolution of large icy satellites. Earth and Planetary Science Letters, 203(1), 399-412.

Simon, F., and Glatzel, G. (1929) Bemerkungen zur Schmelzdruckkurve. Zeitschrift für anorganische und allgemeine Chemie, 178(1), 309–316.

Sinogeikin, S., Bass, J., Prakapenka, V., Lakshtanov, D., Shen, G.Y., Sanchez-Valle, C., and Rivers, M. (2006) Brillouin spectrometer interfaced with synchrotron radiation for simultaneous X-ray density and acoustic velocity measurements. Review of Scientific Instruments, 77(10).

Wagner, W., and Pruss, A. (2002) The IAPWS formulation 1995 for the thermodynamic properties of ordinary water substance for general and scientific use. Journal of Physical and Chemical Reference Data, 31(2), 387-535.

Wiryana, S., Slutsky, L.J., and Brown, J.M. (1998) The equation of state of water to 200 degrees C and 3.5 GPa: model potentials and the experimental pressure scale. Earth and Planetary Science Letters, 163(1-4), 123-130.

Tables

Table 3.1. Measure sound velocities of liquid H_2O

T (K)	Pressure (GPa)	Velocity (km/s)	T (K)	Pressure (GPa)	Velocity (km/s)	T (K)	Pressure (GPa)	Velocity (km/s)
300	0.05	1.581	373	2.4	3.413	523	0.7	2.259
300	0.1	1.613	423	0.6	2.084	523	2.0	3.093
300	0.3	1.891	423	0.8	2.284	523	2.0	3.072
300	0.7	2.365	423	1.0	2.450	523	2.1	3.173
300	1.1	2.694	423	1.2	2.691	523	2.7	3.429
300	1.2	2.699	423	1.6	2.929	523	2.7	3.454
300	1.3	2.853	423	2.0	3.178	523	4.5	4.159
300	1.4	2.883	423	2.5	3.386	523	4.6	4.247
373	0.3	1.853	423	2.8	3.555	723	2.0	2.859
373	0.4	1.938	423	3.0	3.659	723	3.4	3.498
373	1.6	2.899	423	3.1	3.667	723	4.0	3.694
373	2.1	3.212	473	0.7	2.185	723	4.3	3.841
373	2.2	3.300	473	1.8	2.991	723	5.3	4.079
373	2.3	3.362	473	2.5	3.342	723	5.7	4.219
373	2.3	3.382	473	3.7	3.897	723	6.3	4.359

Figures

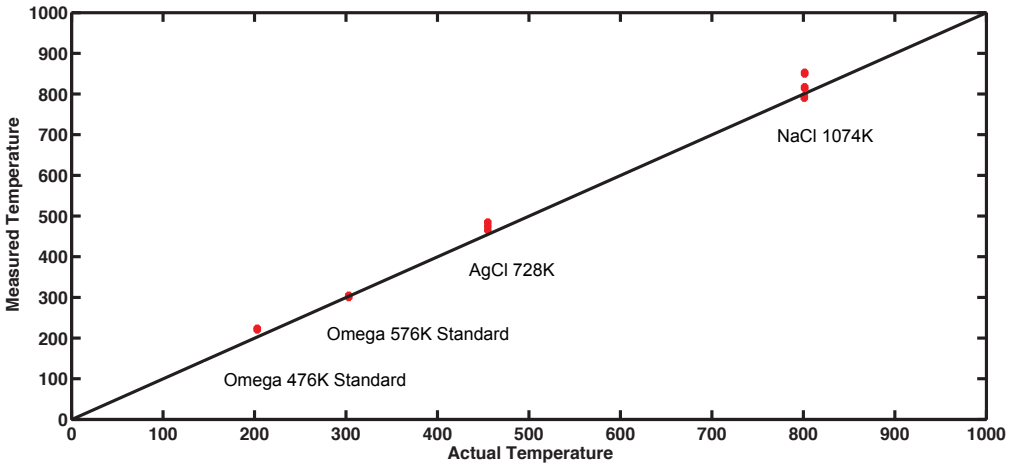

Figure 3.1. High temperature calibration of the membrane DAC using standard materials.

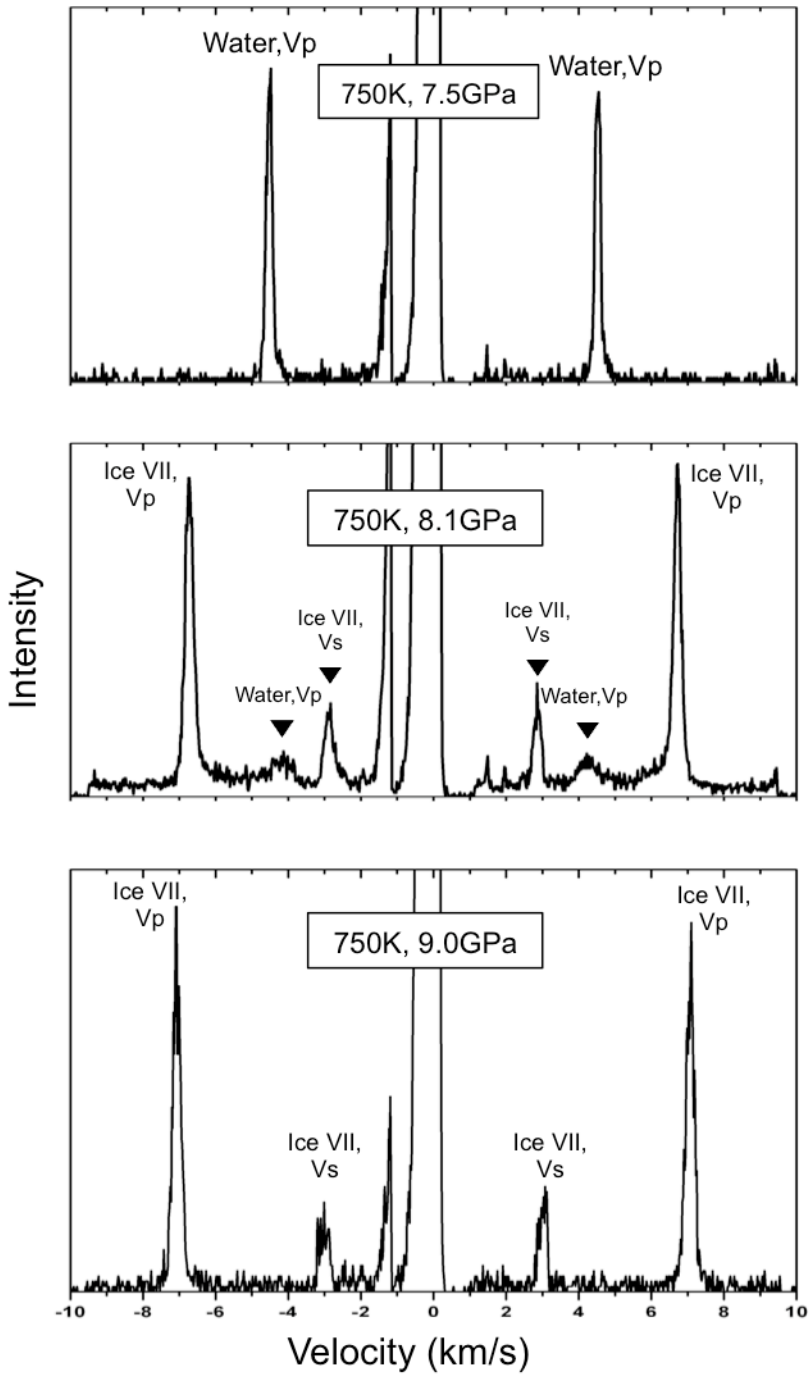

Figure 3.2. Representative profiles of Brillouin scattering upon crystallizing. Spectrums were collected during pressurizing at 750 K.

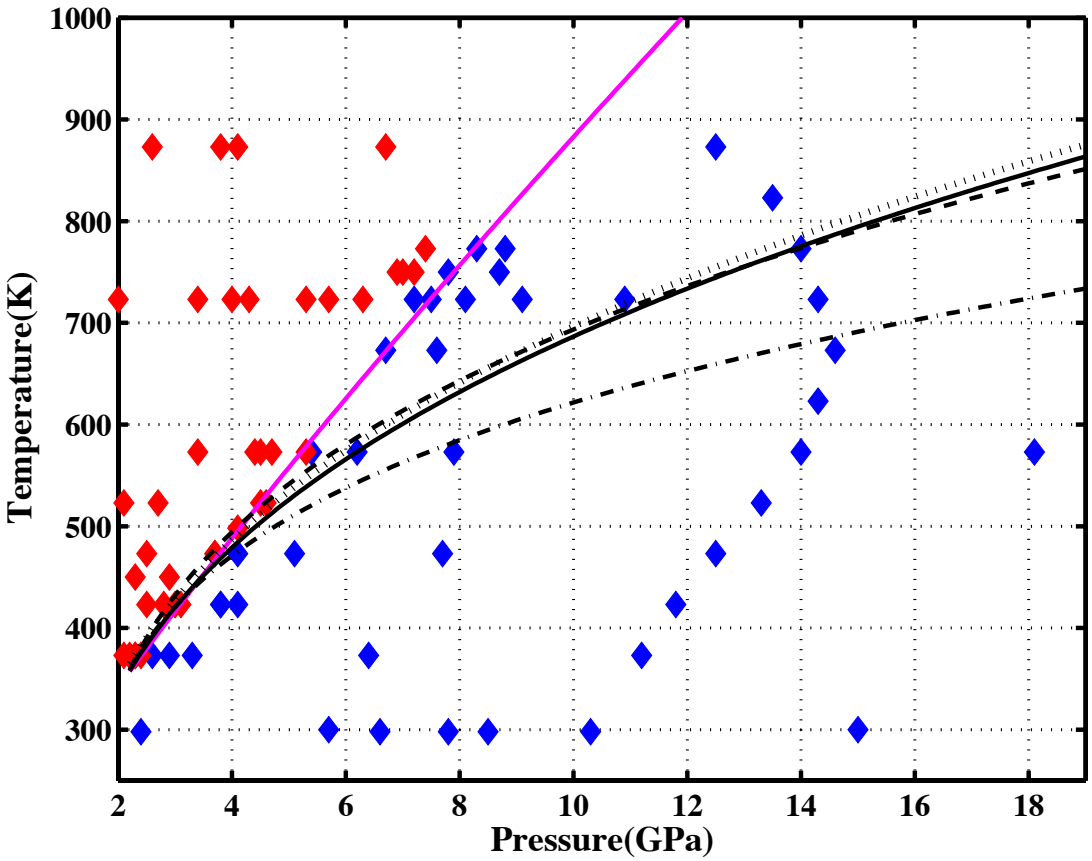

Figure 3.3. Melting curve of Ice VII at high P-T. Blue diamonds and red diamonds represent Ice VII and liquid water of this study. Our fitted melting curve (Magenta solid line) is compared to previous studies: Dubrovinskaia and Dubrovinsky (dotted line) (2003), Lin et al. (dashed line) (2004), Datchi et al. (black solid line) (2000), and Frank et al. (dot-dashed line) (2004).

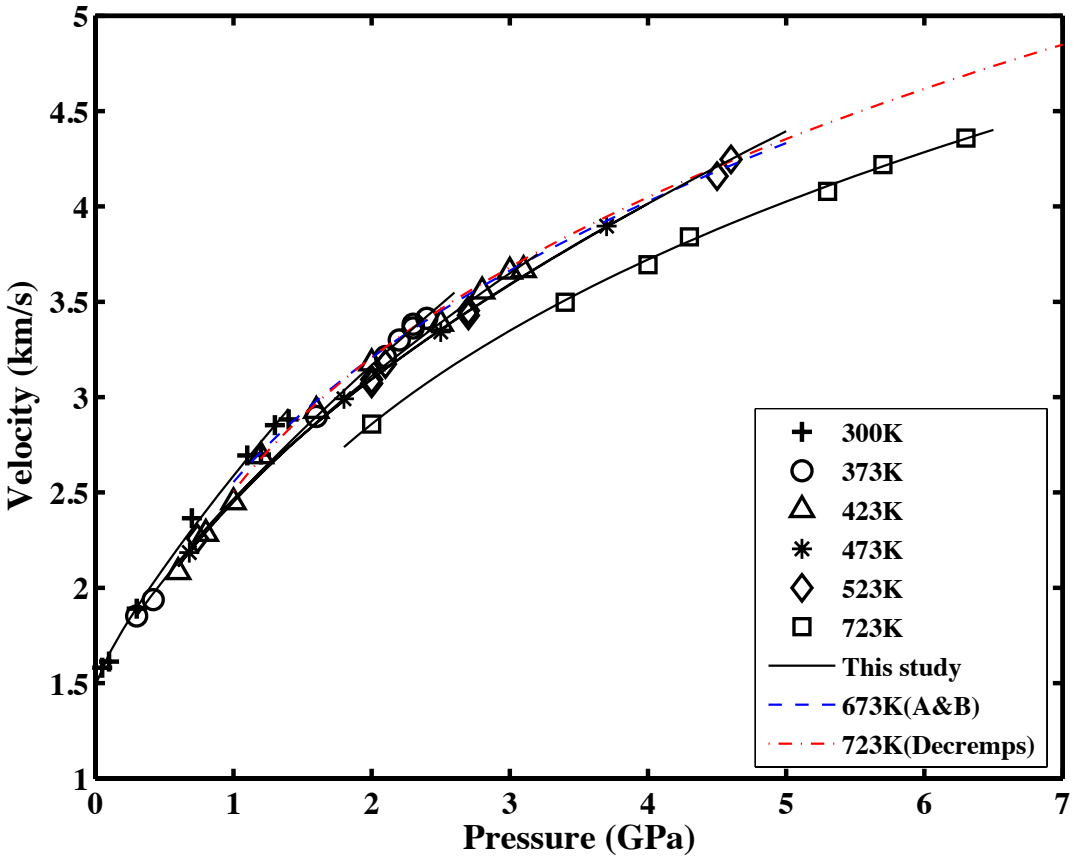

Figure 3.4. The measured sound velocities in liquid H_2O along several isotherms. Solid lines represent the least square power law fitting of the velocity data. A&B: Abramson and Brown (2004); Decremps: Decremps et al. (2006).

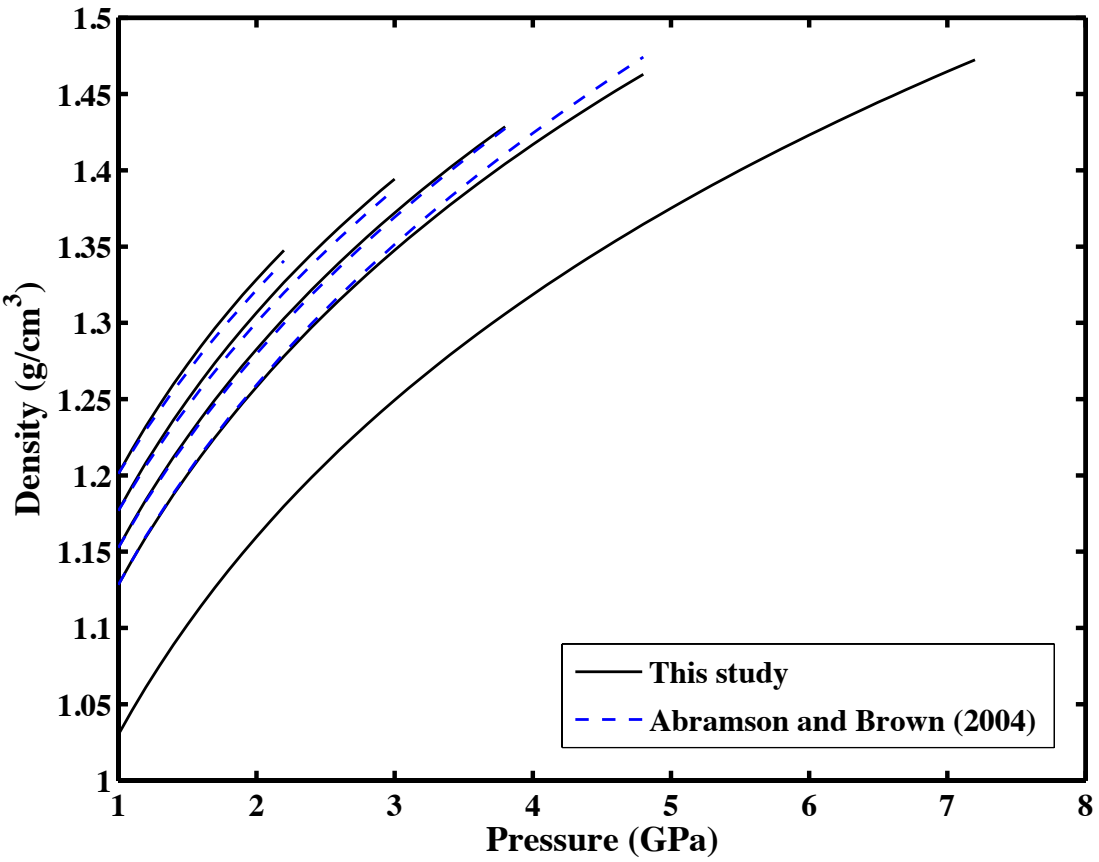

Figure 3.5. Calculated density of liquid H_2O along isotherms of 373, 423, 473, 523 and 723K (from top to bottom). Blue dashed lines represent density curves along isotherms of 373, 423, 473 and 523K (from top to bottom) predicted by the EOS for water from Abramson and Brown (2004).